

# Chemical Kinetics in Microdroplets

Kevin R. Wilson<sup>1,\*</sup> and Alexander M. Prophet<sup>1,2</sup>

<sup>1</sup>*Chemical Sciences Division, Lawrence Berkeley National Laboratory, Berkeley, CA 94720*

<sup>2</sup>*Department of Chemistry, University of California, Berkeley, CA 94720*

## Abstract

Micron-sized compartments play significant roles in driving heterogeneous transformations within atmospheric and biochemical systems as well as providing vehicles for drug delivery and novel reaction environments for the synthesis of industrial chemicals. Many reports now indicate that reaction kinetics are accelerated under micro-confinement; for example in sprays, thin films, droplets, aerosols, and emulsions. These observations are dramatic, posing a challenge to our understanding of chemical reaction mechanisms with potentially significant practical consequences for predicting the complex chemistry in natural systems. Here we introduce the idea of “kinetic confinement,” which is intended to provide a conceptual backdrop for understanding when and why microdroplet reaction kinetics differ from their macroscale analogs.

\*Kevin R. Wilson, [krwilson@lbl.gov](mailto:krwilson@lbl.gov), [orcid.org/0000-0003-0264-0872](https://orcid.org/0000-0003-0264-0872)

Alexander M. Prophet, [aprophet@lbl.gov](mailto:aprophet@lbl.gov)

**Key Words:** *microdroplets, accelerated chemistry, heterogeneous kinetics, multiphase reactions.*

## 1. Introduction

Real world chemistry often occurs heterogeneously, where transformations happen in and on small compartments, such as within atmospheric and combustion aerosol or in cells. Translating the kinetic information obtained from homogeneously mixed laboratory scale reactors to those that occur in small and heterogeneous environments remains a challenge. For multiphase atmospheric chemistry, there are established methods (1-6) to connect rate coefficients measured in homogeneous beaker-scale reactors to those in small droplets and aerosols where surfaces matter. There are now many reports (7-12) that chemistry occurring in microdroplets is somehow fundamentally altered under micro-confinement; raising important questions of how to properly link chemical reactivity between the macro- and microscales.

From textbook chemical kinetics, rate laws for chemical reactions should only depend upon intrinsic properties of the system such as temperature, pressure, ionic strength, reagent concentrations and the rate coefficient. The size of the reaction vessel, an extrinsic property, should not alter the kinetics of a reaction. It is well known, however, that this breaks down when the reaction volumes approach molecular dimensions (*i.e.*, nano-confinement (13)). Quantum dots exhibit altered electronic properties relative to their macroscale analogs, while molecular transport and reactivity within the small spaces of carbon nanotubes, (14) zeolites, nanovessels, (15) metal organic frameworks, and cells lead to properties and behavior different their macroscopic analogs. This is because confinement is on the order of molecular/atomic dimensions or solvent correlation lengths, (16, 17) with systems often exhibiting altered electronic properties and/or stochastic dynamics governed by fluctuations of small numbers of particles (18-22).

This contrasts with micro-confinement (*i.e.*, in micron-sized droplets), where the compartment dimensions encapsulate a relatively large number of solute molecules. These spaces

are much too large to be influenced by nanoscopic confinement effects, so it is often not clear why the micro-confinement would produce behavior substantially different from what is observed in a beaker. Yet there have been many reports of greatly accelerated reactions in microdroplets, thin films, and emulsions relative to the same reactions conducted in macroscopic containers (7, 12). These observations are remarkable, with acceleration factors in excess of  $10^6$  (7). In some cases, reactions that are both thermodynamically and kinetically unfavorable (23-26) in bulk aqueous solutions appear (27, 28) to proceed with minimal reaction barriers in microdroplets. Despite many publications and reviews, (7-12) there appears to be no consensus as to the nature of the acceleration mechanism(s). Likely there are multiple possible mechanisms that depend upon the details of the reaction.

The droplet interface is routinely invoked in mechanistic discussions, with partial solvation, reagent orientation, extremes of surface acidity or basicity, and large electric fields suggested as reasons for an intrinsic increase in the reaction rate constant within microdroplets (7). In many experiments there are additional confounding factors that contribute to the acceleration mechanism, such as the rapid evaporation of reagents and/or solvent, (28, 29) interfering gas phase (27, 28, 30) and wall reactions, (28) which if not carefully controlled in a droplet experiment naturally produce accelerated kinetics.

The goal of this review is to develop a conceptual, kinetics-based framework for evaluating why and when reaction rates in microdroplets might differ from their macroscale analogs. This review will not address the stochasticity of reaction rates that accompany nano-confinement (21, 22) or chemistry in subcellular biological structures (31, 32) where the average concentration corresponds to less than 1 molecule/compartment (18). Instead, the focus is on micron-sized compartments (*i.e.*, droplets with radius,  $r$ ) that contain many molecules; for instance,  $\sim 10^4$  ( $r \sim 1$

$\mu\text{m}$ , [solute]  $\sim 0.01$  mM) and  $\sim 10^{15}$  ( $r \sim 100$   $\mu\text{m}$ , [solute]  $\sim 1$  M). This review will also not provide an exhaustive account of the chemical reactions to date that have been accelerated in microdroplets, the majority of which have been measured by electrospray ionization mass spectrometry (ESI-MS), as reviewed in Refs. (7, 8, 11, 12). This review will also omit discussion of photochemical or photocatalytic reactions that can be accelerated due to the unique ways that light couples to microcavities (33-41).

This review is organized as follows. In Sect. 2, a simple kinetic framework of a droplet is introduced, which is used to explain how characteristic lengths of a chemical reaction lead to the concept of kinetic confinement as described in Sect. 3. In Sect. 4, two examples are used to illustrate how macroscale kinetics are altered in a microdroplet. Sect. 5 concludes with an outlook on future work needed to unravel acceleration mechanisms seen in microdroplet-based chemistry.

## 2. Kinetic Framework

General concepts, throughout this review, are illustrated using the simplified picture of a microdroplet in Figure 1. This framework has been previously implemented in explicit reaction-diffusion kinetic simulations (*i.e.*, Kinetiscope (42)) to predict multiphase reaction rates in droplets, (4, 43, 44) aerosols (45-48) and emulsions (49). This framework formed the basis of a set of closed form equations that link reactions rates measured in beaker scale systems to multiphase reaction kinetics in droplets (4).

In a coarse grain way, a droplet can be described as two kinetically distinct regions or compartments: one representing the interface and the other the droplet interior (*i.e.*, bulk). The thickness of the surface region is assumed to be 1 nm and is selected to be roughly consistent with density and solvation energy profiles of aqueous systems observed in molecular dynamics simulations (MD) (6, 50, 51). The finite thickness of the surface region allows surface-adsorbed

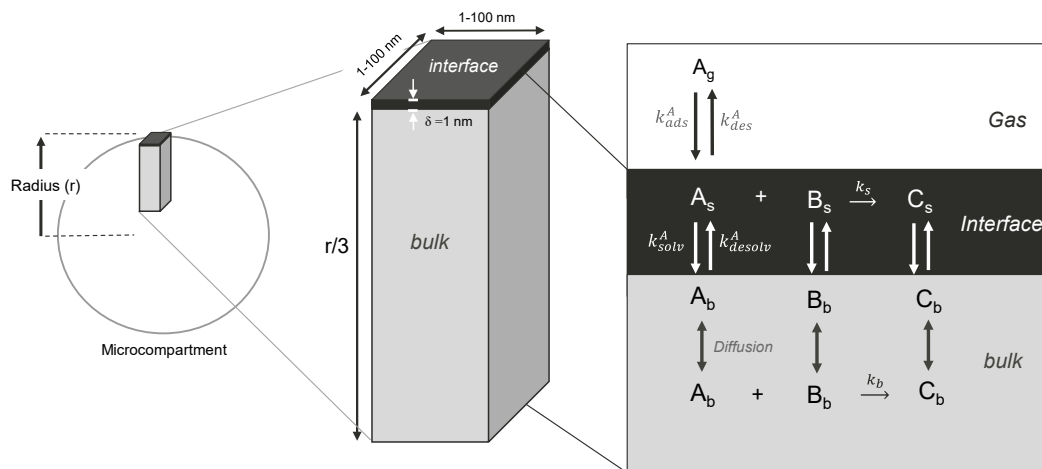


**Figure 1:** Conceptual framework used to describe reaction kinetics in microdroplets. The droplet is simplified into two kinetically active regions or compartments linked by diffusion. Surface partitioning of reagents from the gas (g) and liquid side of the interface are described by a set of adsorption (*ads*), desorption (*des*), solvation (*solv*) and desolvation (*desolv*) rate constants.  $A + B \rightarrow C$  reactions occur both at the surface (s) and bulk (b) regions of the droplet. The interface is assumed to be 1 nm thick and the height of the rectangular prism is  $r/3$  to replicate the surface-to-volume scaling of a sphere with radius,  $r$ . Additional details about this framework including how it is implemented in explicit reaction-diffusion simulations, its limitations and assumptions can be found in Willis and Wilson (43) and Wilson *et al.* (4).

species to be defined using volumetric concentrations. The rectangular prism geometry (47, 48) with a height of  $r/3$  replicates the surface-to-bulk scaling of a sphere. Since compartment volume and reactant concentrations are independent quantities, finite size effects are captured when this framework is implemented in reaction-diffusion simulations (49). Molecules move between compartments by Fickian diffusion and inside each compartment there are a set of elementary steps that correspond to a reaction mechanism. At the interface, additional steps describe the partitioning of reactants A and B between phases (*i.e.*, gas, interface and bulk). These steps are formulated in

a Langmuir framework (52) using a set of rate constants ( $k_{solv}$ ,  $k_{desolv}$ ,  $k_{ads}$ , and  $k_{des}$ ) shown in Figure 1. These rate constants also define characteristic lengths and timescales, which lead to the concept of “kinetic confinement” as will be explained below. This framework is simple and does not resolve chemical gradients in the interfacial or bulk volumes, but rather approximates [A], [B] and [C] in both regions as average quantities. These approximations appear realistic enough to explain (43) many of the kinetic changes that occur when chemistry is transferred from the macro- to microscales.

### 3. Kinetic Confinement of Chemical Reactions at the Microscale.

Not surprisingly, chemistry in microdroplets is heavily influenced by the droplet interface. This is elucidated by introducing the concept of “kinetic” confinement. Unlike nano-confinement,

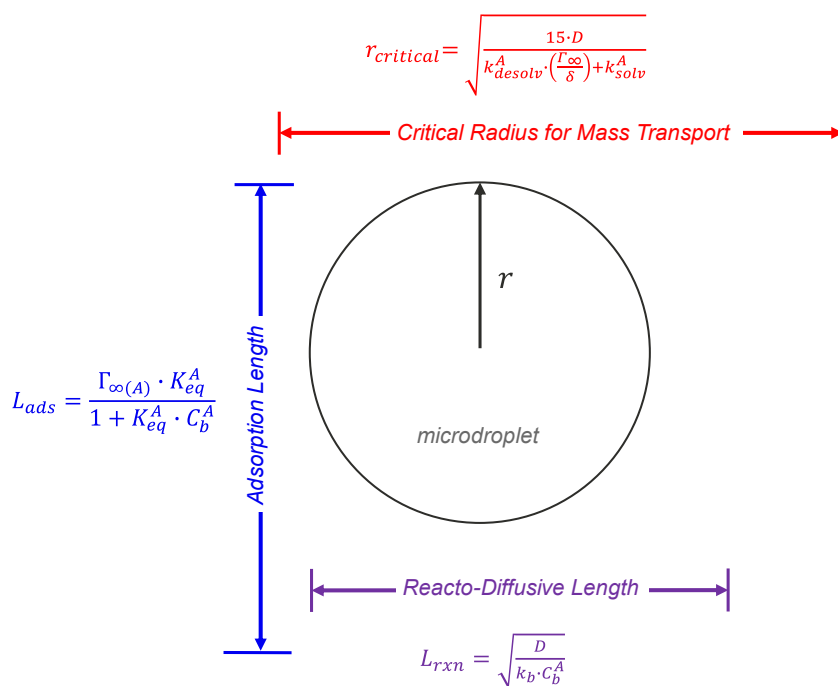


**Figure 2:** Characteristic lengths relative to droplet size ( $r$  = radius). Rate coefficients correspond to the kinetic model shown in Figure 1.  $C_b$  is the bulk concentration of solute A.

where length scales approach molecular dimensions, “kinetic” confinement occurs when the size of the compartment approaches a set of characteristic lengths associated with a chemical reaction.

As shown in Figure 2, these are the reacto-diffusive ( $L_{rxn}$ ) and adsorption ( $L_{ads}$ ) lengths and the critical radius ( $r_{crit}$ ). These characteristic lengths depend upon the familiar factors that govern kinetics, such as concentration, rate and diffusion coefficients (*c.f.*, Figure 1 and 2). The rate constants that describe the partitioning of solutes to and from the interface ( $k_{solv}$  and  $k_{desolv}$ ) figure prominently in these characteristic lengths (Figure 2). The size of the microdroplet relative to these lengths control whether in-droplet chemistry will differ substantially from what is observed in a macroscale reactor. A potentially important additional characteristic length scale in aqueous droplets, not discussed here, is the width of the electric double layer relative to droplet size; a discussion of which can be found in Refs. (53, 54).

**3.1 Fraction of Surface to Bulk Molecules:**  $N_{s/b}$  defines the number of molecules at the interface vs. bulk interior for any given volume, with a comparison of micro- and macro-scales shown in Figure 3. Neglecting partitioning to the gas phase,  $N_{s/b}$  is computed from the number of surface ( $n_s$ ) and bulk ( $n_b$ ) molecules,

$$N_{s/b} = \frac{n_s}{n_b} = \frac{C_s^A}{C_b^A} \cdot \frac{V_s}{V_b}, \quad (1)$$

where  $C_s$  and  $C_b$  are the solute concentrations of A at the surface ( $s$ ) and bulk ( $b$ ) of the droplet.  $V_b$  is the volume of the droplet and  $V_s$  is the interfacial volume. For a sphere,

$$V_s = V_b - \frac{4}{3} \pi (r - \delta)^3 \quad \text{and} \quad V_b = \frac{4}{3} \pi r^3 \quad (2)$$

such that,

$$\frac{V_s}{V_b} = \frac{r^3 - (r - \delta)^3}{r^3} \approx \frac{3 \cdot \delta}{r}. \quad (3)$$

$\delta$  is interface thickness and is assumed to be 1 nm. For a Langmuir isotherm,  $C_s^A$  is a function of the bulk concentration,

$$C_s^A = \frac{\Gamma_{\infty(A)}}{\delta} \cdot \frac{K_{eq}^A \cdot C_b^A}{1 + K_{eq}^A \cdot C_b^A} \quad (4)$$

$$K_{eq}^A = \frac{k_{desolv}^A}{k_{solv}^A} \quad (5)$$

where  $\Gamma_{\infty}$  is the maximum surface concentration (molec./cm<sup>2</sup>).  $K_{eq}^A$  (cm<sup>3</sup>/molec.) is the Langmuir equilibrium constant and is expressed as the ratio of desolvation ( $k_{desolv}$ , cm<sup>3</sup>/molec./s) and

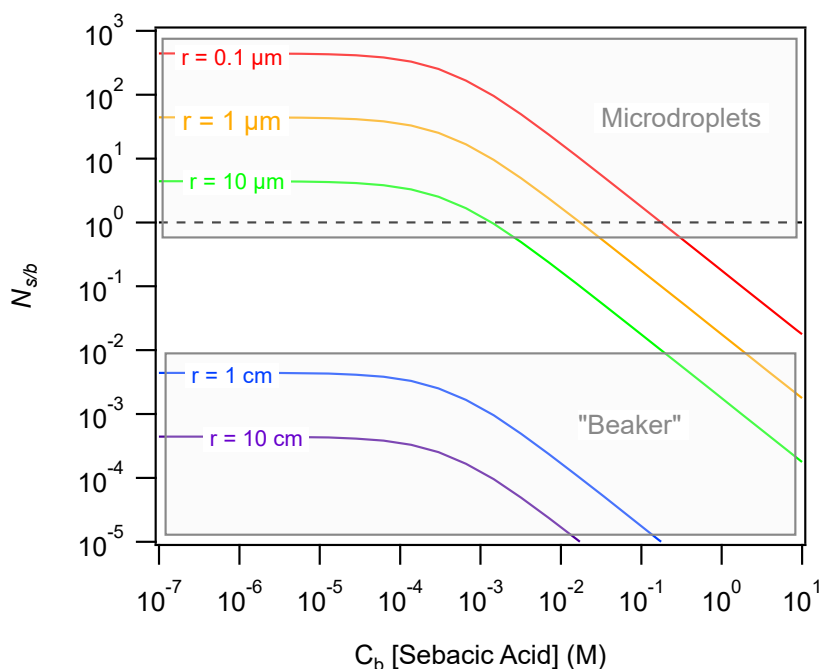


**Figure 3:**  $N_{s/b}$  vs. concentration of bulk sebacic acid ( $C_b$ ) and droplet size (Equation 1). Boxed shaded areas show the difference between microdroplets and “beaker” scale reactors modeled using  $r = 1$  and 10 cm droplets.

solvation ( $k_{solv}$ , 1/s) rate coefficients as shown in Figure 1. The following discussion is made more concrete by using sebacic acid ( $C_{10}H_{18}O_4$ ) as an example solute (*i.e.*, A).  $k_{desolv}^A$  ( $2 \times 10^{-16}$  cm<sup>3</sup>/molec./s),  $k_{solv}^A$  (48 1/s) and  $\Gamma_{\infty}$  ( $1.5 \times 10^{14}$  molec./cm<sup>2</sup>) were previously measured for sebacic

acid solutions by Bleys and Joos (55). As shown in Figure 3, there is a significant difference in  $N_{s/b}$  for microdroplets compared to beaker scale containers. On average only a small fraction ( $10^{-3}$  to  $10^{-5}$ ) of the total number of solute molecules reside at the interface of a “beaker” scale solution, which is modeled as large droplets with  $r = 1$  or  $10$  cm. This is not the case for microdroplets where, depending on concentration and size, a substantial portion ( $0.1$  to  $10^2$ ) of the total molecules in a droplet reside at the interface. This is simply a consequence of the small volume of microdroplets, which require fewer numbers of solute molecules to achieve the same concentration as in a macroscale beaker.

A larger  $N_{s/b}$  for microdroplets doesn't necessarily mean that chemical reactions are accelerated, since reaction rates depend on concentration and not number. However, when microdroplets are viewed as a reactive “system” comprised of both surface and bulk environments, reaction acceleration can occur if interfacial concentrations, reaction rates or equilibria are substantially different than those in the droplet interior. In these cases, a larger  $N_{s/b}$  will mean that a larger fraction of the total molecules in the droplet will cycle through the interface producing a much greater sensitivity to the difference in the reactivity of the bulk and surface environments. As will be shown below for chemical equilibria,  $N_{s/b}$  acts as an interface weighting factor, which is small for macroscale compartments but becomes sizeable when droplets are small and reactants are dilute.

Large values of  $N_{s/b}$  will also mean that the overall outcome of a chemical reaction in a microdroplet will be much more sensitive to those non-reactive steps of solvation and desolvation ( $k_{solv}$  and  $k_{desolv}$  in Figure 1) that kinetically link the interface with the bulk. In other words, large values of  $N_{s/b}$  produce strong coupling between the surface-partitioning equilibria of A and B and the surface and bulk reaction steps ( $k_s$  and  $k_b$ , Figure 1) that form product C. While the coupling

of these elementary steps and equilibria certainly occurs at the macroscale air-liquid interface, their influence on the overall chemical evolution of the system is obscured by the small fraction of interfacial molecules ( $N_{s/b} \sim 10^{-4}$ ). Only surface selective probing by techniques, such as sum frequency and second harmonic generation, can isolate these interfacial dynamics from the large background of molecules in the bulk liquid. This suggests that atomizing a bulk solution into many small microdroplets is an effective way to isolate and observe the role of the interface using detection techniques that are not inherently interface sensitive.

**3.2 Adsorption length ( $L_{ads}$ ):**  $L_{ads}$  is a common metric used in the surfactant literature (56) to describe the distance over which an interface draws solute from the bulk solution to maintain its equilibrium coverage,

$$L_{ads} = \frac{c_s^A \cdot \delta}{c_b^A} = \Gamma_{\infty(A)} \cdot \frac{K_{eq}^A}{1 + K_{eq}^A \cdot c_b^A}. \quad (6)$$

From Equation (1),  $L_{ads}$  can be written in terms of the surface fraction  $N_{s/b}$ ,

$$L_{ads} = \frac{V_b}{V_s} \cdot N_{s/b} \cdot \delta = \frac{r}{3} \cdot N_{s/b}, \quad (6a)$$

illustrating the direct relationship between  $L_{ads}$ ,  $r$  and surface fraction  $N_{s/b}$ . Equation (6a) implies an adsorption length greater than the  $r/3$  necessitates  $N_{s/b} > 1$ . If the surface is saturated then  $L_{ads}$  is,

$$L_{ads}^{sat.} = \frac{\Gamma_{\infty(A)}}{c_b^A}. \quad (6b)$$

In the low concentration limit of  $c_b^A$ ,  $L_{ads}$  approaches a maximum length,

$$L_{ads}^{max.} = \Gamma_{\infty(A)} \cdot K_{eq}^A. \quad (6c)$$

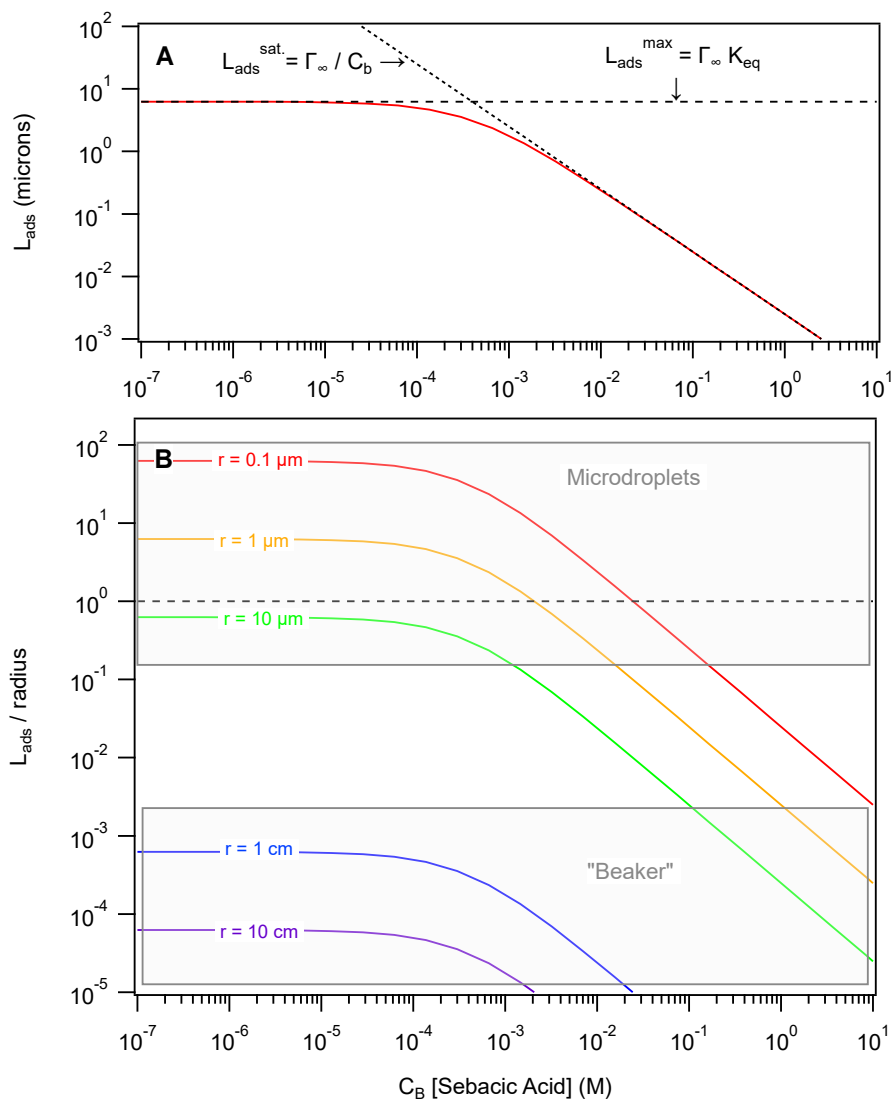


**Figure 4:** (A) Adsorption length ( $L_{ads}$ ) vs. bulk [sebacic acid] computed using Equation 6 (red line). Dotted line (Equation 6b) shows  $L_{ads}^{sat}$ , while dashed line (Equation 6c) indicates the maximum adsorption length. (B)  $L_{ads}/r$  vs. bulk [sebacic acid]. Dashed line indicates  $L_{ads}/r = 1$ . Boxed shaded areas show the difference between microdroplets and “beaker” scale reactors modeled using  $r = 1$  and  $10$  cm droplets.

As shown in Figure 4A for an aqueous solution of sebacic acid, these adsorption lengths can be microns ( $L_{ads} = 6.2$  microns) at small concentrations ( $10^{-7}$  M), which decreases to many nanometers for [sebacic acid]  $> 1$  mM. The functional form of  $L_{ads}$  vs. concentration merely reflects the nonlinear relationship between  $C_S$  and  $C_B$  in the Langmuir equation (Equation 4). Figure 4B shows

the ratio of adsorption length to radius vs.  $C_b$ ; illustrating, once again, the substantial differences (i.e.,  $10^3 - 10^5$ ) between microdroplets and macroscale containers. For macroscopic droplets ( $r = 1-10$  cm)  $L_{ads}/r < 10^{-3}$ . In contrast, for droplet radii  $< 10$   $\mu\text{m}$  and  $C_b < 10^{-2}$  M,  $L_{ads}/r$  is  $\geq 1$  (see dashed line, Figure 4B) indicating that the adsorption length is on the order or larger than the droplet dimensions. This means that there is not enough solute within the finite droplet volume to sustain the same macroscale equilibrium between the surface and bulk solute concentrations. In other words, for  $L_{ads} > r$  the microdroplet bulk and surface concentrations (57) are depleted relative to those at the macroscale, which has clear consequences for altering reaction kinetics in both locations. For the opposite case,  $L_{ads} < r$ , the interface is a negligible perturbation and does not lead to any substantial differences in solute partitioning between microdroplets and their macroscopic analogs.

A dramatic manifestation of droplet size relative to  $L_{ads}$  is observed by comparing the surface tension of microdroplets to macroscopic flat surfaces as shown by Bzdek and coworkers (58, 59). Shown in Figure 5A are static surface tension measurements for a 0.5 M aqueous sodium

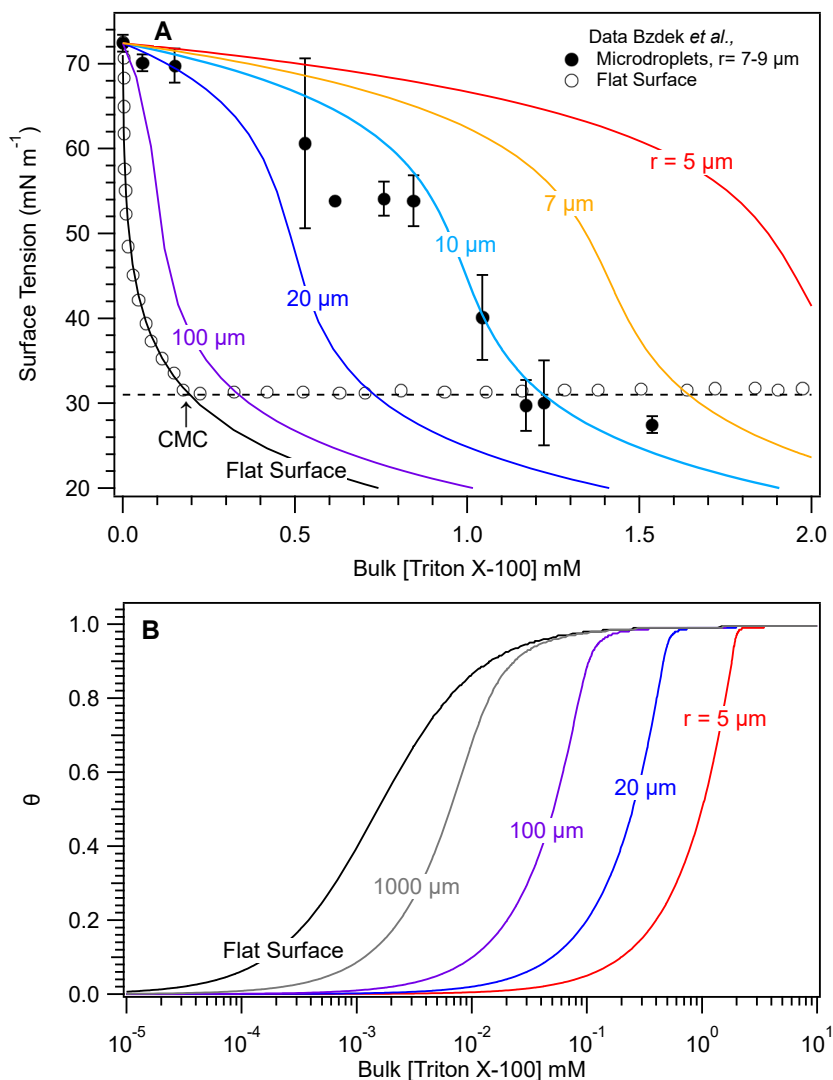


**Figure 5:** (A) Surface tension vs. bulk [Triton X-100]. Flat surface (○) and microdroplet data (●) reported by Bzdek *et al.* (58). Lines show predictions for the size dependent surface tension in droplets (see Equations 7 and 12). The critical micelle concentration (CMC) is denoted with a dashed line. (B) Fractional surface coverage ( $\theta$ ) as a function of bulk [Triton X-100] for a flat surface (Equations 7 and 8) and as a function of microdroplet radius (see Equations 7 and 12).

chloride solution as a function of the [surfactant] (*i.e.*, Triton X-100). Bzdek *et al.*, (58) observed a large difference in the scaling of surface tension with [Triton X-100] for a flat surface vs.  $r = 7\text{--}9$  μm droplets (as shown in Figure 4 of their publication and shown in Figure 5A). At [Triton X-

100] = 0.2 mM the surface tension of the flat surface is at a minimum (30 mN m<sup>-1</sup>) and near the critical micelle concentration (CMC). Alternatively, the surface tension of  $r = 7\text{-}9\ \mu\text{m}$  droplets at the same concentration is much larger and near that of pure water ( $\sim 72\ \text{mN m}^{-1}$ ). Below these differences are explained quantitatively by accounting for the modified solute partitioning behavior in microdroplets.

The flat surface tension data in Figure 5A is fit to the Szyszkowski equation of state (60) to obtain the Langmuir equilibrium constant,  $K_{eq}^A$ ,

$$\gamma - \gamma_{water} = \Gamma_{\infty}^Y \cdot R \cdot T \cdot \ln(1 - \theta), \quad (7)$$

where,

$$\theta = \frac{C_S^A}{\frac{\Gamma_{\infty}}{\delta}} = \frac{K_{eq}^A \cdot C_b^A}{1 + K_{eq}^A \cdot C_b^A}. \quad (8)$$

$\theta$  is fractional surface coverage.  $\gamma$  and  $\gamma_{water}$  are the surface tensions of the solution and pure water, respectively.  $R$  is the gas constant and  $T$  is temperature. A fit of Equation 7 to the flat surface data yields  $K_{eq}^A = 1.1 \times 10^{-15}\ \text{cm}^3/\text{molec.}$  and  $\Gamma_{\infty} = 2 \times 10^{14}\ \text{molec./cm}^2$ . These values correspond to  $L_{ads} = 16.5\ \mu\text{m}$  at [Triton X-100] = 0.2 mM (*i.e.*, at the CMC), which is similar to the droplet size. This means that the surface coverage of the surfactant in a microdroplet is no longer described simply by Equation 8, since the bulk droplet concentration will be substantially perturbed by its interface. Instead,  $C_S^A$  is obtained using a set of equations and the rate coefficients for surfactant desolvation and solvation. At equilibrium, the desolvation and solvation rates are equal,

$$k_{desolv} \cdot C_b^A \cdot [site] = k_{solv} \cdot C_S^A, \quad (9)$$

where concentration of empty surface sites is,

$$[site] = \frac{\Gamma_{\infty(Y)}}{\delta} - C_S^A, \quad (10)$$

and the total surfactant concentration in the droplet is,

$$C_{b0}^A = C_b^A + \frac{3 \cdot \delta}{r} \cdot C_S^A. \quad (11)$$

$C_{b0}^A$  is the initial bulk concentration of surfactant prior to its repartitioning inside the droplet. Equation 10 conserves the total site concentration, while Equation 11 conserves the total concentration of surfactant molecules in the droplet. The concentration of adsorbed surfactant  $C_S^A$  in Equation 11 is weighted by  $3\delta/r$  to account for the surface-to-volume ratio of the droplet. Solving Equations 9-11 yields an expression for the equilibrated surfactant concentration at the droplet interface,  $C_S^A$ ,

$$C_S^A = \frac{1}{2 \cdot N_1} \cdot \left( -N_2 - \sqrt{N_2^2 - 4 \cdot N_1 \cdot N_3} \right), \quad (12)$$

where,

$$N_1 = 3 \cdot k_{desolv} \cdot \delta^2 \quad (12a)$$

$$N_2 = -3 \cdot k_{desolv} \cdot \Gamma_{\infty(A)} \cdot \delta - k_{desolv} \cdot C_{b0}^A \cdot \delta \cdot r - k_{solv} \cdot \delta \cdot r \quad (12b)$$

$$N_3 = k_{desolv} \cdot \Gamma_{\infty(A)} \cdot C_{b0}^A \cdot r \quad (12c)$$

Equation 12 is similar to the one derived by Alvarez *et al.* (61). Equation 12 is plotted vs. [Triton X-100] in Figure 5B and clearly shows that the surfactant concentration (*i.e.*, surface coverage  $\theta$ ) is a strong function of droplet size. Surface saturation for a  $r = 5 \mu\text{m}$  droplet occurs at 1 mM, whereas a macroscale solution saturates at  $\sim 0.01$  mM. This difference is a consequence of the relatively small number of solute molecules in a droplet vs. a macroscale solution. It is only when

the droplet is larger than  $L_{ads}^{max}$ . (Equation 6c) does it have a required number of surfactant molecules to achieve the same partitioning behavior of a macroscale system for all surfactant concentrations. In other words, a droplet with radius  $r > L_{ads}^{max}$  will always have  $N_{s/b} < 1$ , and hence, will display adsorption equilibrium behavior consistent with its macroscopic analog.

This then explains the large differences between the flat surface and droplet surface tensions observed by Bzdek *et al.* (58) for droplet sizes far below  $L_{ads}^{max}$ . The droplet surface tension is computed by substituting the expression for  $C_s^A$  (Equation 12) into Equation 7 to compute surface tension vs. droplet size and  $C_b^A$  as shown in Figure 5A. The calculation does a reasonable job replicating the functional form of the droplet measurements reported by Bzdek *et al.* (58) and achieves near quantitative agreement within experimental error at  $r = 10 \mu\text{m}$ , which is slightly larger than the size range ( $r = 7\text{-}9 \mu\text{m}$ ) reported in the experiment.

This analysis shows that for the same solute concentration the surfaces of microdroplets can be quite different from their macroscopic analogs (57). To achieve the same surface tension in a  $r = 5 \mu\text{m}$  droplet as for a flat surface with  $\mu\text{M}$  Triton X-100 concentration requires  $\sim 1000\text{x}$  the surfactant concentration. It is also important to note that unlike the macroscale, both the surfactant concentration and droplet size must be specified to compute surface tension. This is a compelling example where extrinsic factors (container size) play a significant role in the observed properties of microdroplets.

**3.3 Reacto-Diffusive Length ( $L_{rxn}$ ):** Another characteristic length, important for chemistry in microdroplets, is the reacto-diffusive length ( $L_{rxn}$ ),

$$L_{rxn} = \sqrt{\frac{D}{k_b \cdot C_B^A}}. \quad (13)$$

The reacto-diffusive length ( $L_{rxn}$ ), similar to the Kuramoto Length, (62) Damköhler number and reaction diffusion index, (63) is the average distance a molecule travels prior to reaction.  $L_{rxn}$  scales with the square root of the diffusion coefficient ( $D$ ) and the chemical lifetime ( $\tau_{rxn} = (k_{rxn} \cdot C_B^A)^{-1}$ ). For a bimolecular reaction  $L_{rxn}$  can be modulated via reactant concentration. When reactions are slow relative to diffusion,  $L_{rxn} > r$ , reagents can sample the surface region of the microdroplet repeatedly prior to a reaction. For this situation, the observed microdroplet kinetics will be governed both by its bulk and interfacial environments. For fast reaction rates and correspondingly slower diffusion rates (*i.e.*,  $L_{rxn} < r$ ), the surface will likely play a more modest role as reagents, on average, will be consumed prior to encountering an interface. For multiphase reactions where one reagent enters the droplet from the gas phase,  $L_{rxn}$  plays a significant role in both determining where the heterogeneous reaction occurs and for the formation of concentration gradients for the case where  $L_{rxn} \leq r$ . These questions are explored in depth by Limmer *et al.*, (64) in an article appearing in this issue.

**3.4 Critical Radius for Mass Transport:** A critical radius ( $r_{crit}$ ) is used to describe the mode of mass transfer to a curved interface (*i.e.*, bubble or droplet), (56) which can either be diffusively or kinetically controlled. As derived by Klein and Born (65) and later by Mondal *et al.*, (66) the mean first passage time of a molecule uniformly distributed in a bulk droplet to reach the surface is,

$$\langle \tau_{diffusion} \rangle = \frac{r^2}{15 \cdot D} \quad (14)$$

Diffusion times in microdroplets are fast relative to beakers. For example,  $\langle \tau_{diffusion} \rangle \approx 2$  ms for a  $r = 2 \mu\text{m}$  droplet, using a liquid phase diffusion constant of  $D = 8.0 \times 10^{-6} \text{ cm}^2/\text{s}$ .

In the Langmuir framework, (61) the characteristic time for the kinetic transfer of a molecule from the bulk to the surface is,

$$\langle \tau_{sb} \rangle = \frac{1}{k_{desolv} \cdot \left( \frac{r_{\infty}}{\delta} \right) + k_{solv}}. \quad (15)$$

Unlike  $\tau_{diffusion}$ , which is size dependent, the magnitude of  $\tau_{sb}$  depends only on how surface active a solute might be. For sebacic acid, shown in Figs. 3 and 4,  $\langle \tau_{sb} \rangle = 3 \mu\text{s}$ , which is orders of magnitude faster than the diffusion time in a  $r = 2 \mu\text{m}$  droplet.

$r_{crit}$  is the droplet size where the diffusional (Equation 14) and kinetic (Equation 15) timescales are equal (*i.e.*,  $\langle \tau_{diffusion} \rangle = \langle \tau_{sb} \rangle$ ),

$$r_{crit} = \sqrt{\frac{15 \cdot D}{k_{desolv} \cdot \left( \frac{r_{\infty}}{\delta} \right) + k_{solv}}}. \quad (16)$$

For the sebacic acid example,  $r_{crit} = 0.2 \mu\text{m}$ . In this case, mass transfer of solute to the droplet interface ( $r > r_{crit}$ ) will be limited by diffusion and for very fast surface reactions could limit the overall rate. Alternatively, in nanosized droplets ( $r < r_{crit}$ ) the kinetics of solvation will play a more prominent role in the reactive outcome. For multiphase reactions in droplets where one reactant enters the droplet from the gas phase there is an additional critical radii that describes the competition of diffusion with the kinetic steps of gas phase adsorption and desorption shown in Figure 1 and further discussed in Wilson *et al.* (4).

The timescales for surface partitioning of solutes in droplets provides a useful constraint in interpreting the kinetic viability of certain acceleration mechanisms proposed in the literature. For example, if the droplet surface is invoked as part of the acceleration mechanism, then the timescale for reagent partitioning to the interface is likely an important quantity. Some of the large acceleration factors reported in ESI droplets have correspondingly short microsecond reaction

times that are on the order or much faster than the characteristic timescales for mass transfer to the aqueous interface (*i.e.*,  $\mu\text{s}$  to  $\text{ms}$ ). Additionally, for polydisperse droplet distributions, like those produced in many ESI experiments, it is likely that there is a large difference (*e.g.*, 1000x) in the partitioning timescales between the submicron and supermicron droplet populations. Finally, the discussion above only applies to quiescent droplets of a fixed size, which does not strictly describe ESI droplets that are rapidly evaporating and/or undergoing fission events. In this case, the droplet interface is highly dynamic and receding at rates that could exceed diffusion, which requires a more sophisticated analysis and modeling framework such as that described recently by Hardy *et al.* (67).

**3.5 Reaction Rates in Droplets:** Cooks and coworkers, (68) observed that the “reaction molecularity” (*i.e.*, number of reagent molecules involved in the reaction) has a strong influence on which reactions are accelerated in microdroplets. Bimolecular condensation or addition

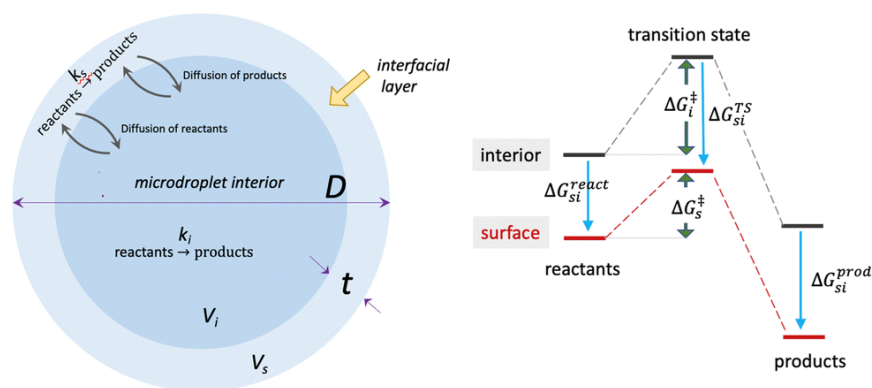


**Figure 6:** Kinetic model (left) and energy diagram (right) developed by Ruiz-Lopez *et al.* (69). Subscript  $i$  denotes the droplet interior (*i.e.*,  $V_i = V_b$  and  $k_i = k_b$ ).  $D$  is the droplet diameter and  $t$  is interface thickness (*i.e.*,  $t = \delta$ ). Figure reproduced from Ref. (69) with permission from the PCCP Owner Societies.

reactions exhibit large acceleration factors, whereas unimolecular decarboxylation and dehydration reactions do not. By comparing canonical energy profiles for gas, interface, and bulk

reactions they hypothesized that this effect could be explained by differential solvation of the reactants and transition states at the gas-liquid interface of droplets (see Figure 2 and Figure S10 in Ref. (68)). Ruiz-Lopez *et al.* (69) presented a kinetic model of microdroplet chemistry that uses Transition State Theory (TST) to explain possible differences in reaction rates occurring at the microdroplet interface and in the bulk. A schematic of their model is shown in Figure 6, where they adopt a similar coarse grain view of a microdroplet shown in Figure 1; a two-compartment system with surface and bulk sub-volumes. Using the adsorption free energy of reactants, they link TST with the thermodynamic partitioning of reactants to the interface. Their model explicitly neglects kinetic and diffusive limitations for the transport of reactants between the bulk and droplet interface. They also assume, for simplicity, that  $L_{\text{ads}} \ll r$ . The acceleration factor (AF) for reactions in microdroplets vs. bulk reactors is, (68, 69)

$$AF = \frac{k_{\text{droplet}}^{\text{eff}}}{k_b}, \quad (17)$$

where  $k_{\text{droplet}}^{\text{eff}}$  is the effective rate constant for the microscale reaction and  $k_b$  is the bulk macroscale rate coefficient (denoted  $k_i$  in Figure 6) for the corresponding reaction. For a unimolecular reaction,  $A \rightarrow C$ ,

$$AF = \frac{k_{\text{droplet}}^{\text{eff}}}{k_{\text{bulk}}} = \frac{\left(1 + \frac{V_s}{V_b} \cdot (K_{sb}^{TS} - 1)\right)}{\left(1 + \frac{V_s}{V_b} \cdot (K_{sb}^A - 1)\right)}, \quad (18)$$

and for a bimolecular reaction  $A + B$ ,

$$AF = \frac{k_{\text{droplet}}^{\text{eff}}}{k_{\text{bulk}}} = \frac{\left(1 + \frac{V_s}{V_b} \cdot (K_{sb}^{TS} - 1)\right)}{\left(1 + \frac{V_s}{V_b} \cdot (K_{sb}^A - 1)\right) \cdot \left(1 + \frac{V_s}{V_b} \cdot (K_{sb}^B - 1)\right)}. \quad (19)$$

$\frac{V_s}{V_b}$  is the ratio of surface to bulk (denoted  $V_i$  in Figure 6) volumes in the droplet.  $K_{sb}^A$ ,  $K_{sb}^B$ , and  $K_{sb}^{TS}$  are the dimensionless surface-to-bulk partitioning coefficients for species A, B, and the Transition State (TS), respectively. Partitioning coefficients depend upon the free energy ( $\Delta G_{sb}$ ) change for a molecule to adsorb to the surface,

$$K_{sb} = \frac{c_s}{c_b} = e^{\frac{-\Delta G_{sb}}{R \cdot T}}. \quad (20)$$

$K_{sb}^{TS}$  is related to the bulk ( $k_b$ ) and surface ( $k_s$ ) bimolecular reaction rate coefficients via,

$$K_{sb}^{TS} = \frac{k_s}{k_b} \cdot K_{sb}^A \cdot K_{sb}^B. \quad (21)$$

As discussed by Ruiz-Lopez *et al.* (69) this model and accompanying equations (Equations 18-21) predicts that for significant reaction acceleration to occur requires that either of the reactants and/or the transition state be stabilized at the droplet interface. The model predicts, depending upon the magnitude of both the partitioning constants and rate coefficients, reaction acceleration of both bimolecular and unimolecular reactions in microdroplets. Although, the magnitude is much smaller in the case of unimolecular reactions in general agreement with the arguments presented by Cooks and coworkers (68).

Model predictions (*i.e.*, Equation 19) as a function of  $r$  are shown in Figure 7. Bimolecular acceleration factors are computed for two scenarios. The first, shown in Figure 7A, assumes that  $\Delta G_{sb} = -4.1$  kcal/mol and is the same for reactants A and B. The resulting AF is plotted vs.  $r$  for different ratios of surface-to-bulk rate coefficients. Even when  $k_s/k_b \leq 1$  the in-droplet reaction exhibits ~10X acceleration for  $r \sim 1$ -10 microns. This is simply a consequence of the surface enrichment of A and B and therefore the transition state species. As  $k_s/k_b$  increase, substantial AF factors ( $10^4$ ) are predicted to occur in microdroplets.

The second scenario is shown in Figure 7B, where AF's are plotted vs. droplet size as a function of  $\Delta G_{sb}$ . Here we assume  $k_s = 10 \cdot k_b$ . The AF increases with increasingly negative values of  $\Delta G_{sb}$ ; corresponding to greater enrichment of A and B at the interface. The peak in the AF shifts to larger  $r$ , which reflects the difference in scaling of the numerator and denominator of Equation 19 with droplet size. Again, microdroplets are predicted to have substantial AF's ( $\sim 10^4$ ) with only

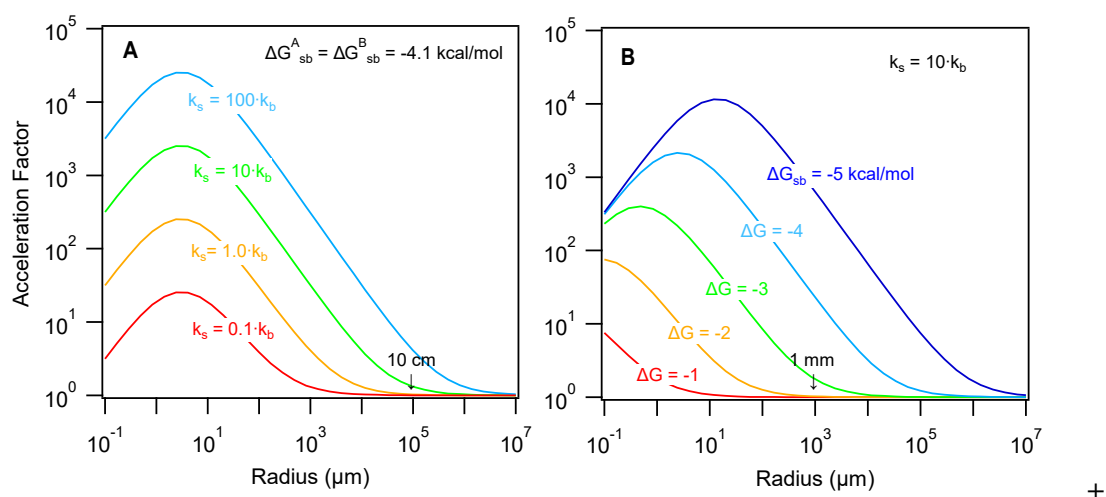


**Figure 7:** Computed acceleration factor (AF, Equation 19) vs. droplet radius as a function (A)  $k_s/k_b$  for  $\Delta G_{sb} = -4.1 \text{ kcal mol}^{-1}$  and as a function of (B)  $\Delta G_{sb}$  for  $k_s = 10 \cdot k_b$ . Arrows show  $r = 10 \text{ cm}$  (A) and  $1 \text{ mm}$  (B).

a modest increase (*i.e.*, 10x) in the rate coefficient for the interfacial reaction. This factor of 10 in  $k_s$  vs.  $k_b$  could, for example, reflect changes in the solvation environment at the interface. Substantially larger ratios (*i.e.*,  $k_s/k_b > 1000$ ) and  $\Delta G_{sb} (> -7 \text{ kcal/mol})$  are needed to replicate the extremely large AF's ( $10^5$ - $10^6$ ) observed to date as discussed by Ruiz-Lopez *et al.* (69).

One interesting prediction afforded by the kinetic model of Ruiz-Lopez *et al.* (69) is that AF's  $> 1$ , in some cases, should be readily observable in rather large droplets or compartments. From Figure 7A, for  $k_s = 100 \cdot k_b$ , AF's between 4 and 300 should be observable in  $r \sim 10 \text{ cm}$  and  $1 \text{ mm}$  droplets, respectively. These sizes are generally considered macroscale and thus should be

relatively easy to measure using conventional instrumentation. Additionally, if the very large AF's reported previously are correct then significant reaction acceleration should be visible in these larger sample containers. This may explain why AFs in larger Leidenfrost droplets are consistently smaller than in droplets formed by electrospray (70). Extrapolations to large sizes shown in Figures 7A and 7B are likely to be an over-estimate, since liquid phase diffusion (explicitly neglected in Equation 19) likely limits the transport rate of reagents to and from interface in large droplets (*i.e.*,  $r > r_{crit.}$ ) as described above.

#### 4. Exemplars

Below the concepts of “kinetic confinement” are illustrated using two examples. Both examples focus on experiments where the droplet size is carefully controlled and characterized, which allows realistic kinetic models to be constructed to inform experimental observations. Kinetic models of these experiments were formulated by our group (43, 49) using the framework shown in Figure 1. The first example involves the multiphase reaction of O<sub>3</sub> and aqueous nitrite (NO<sub>2</sub><sup>-</sup>) to produce nitrate (*i.e.*, a simple A + B → C reaction). This example is also intended to provide a connection between the emerging field of microdroplet accelerated chemistry and the more mature work on multiphase atmospheric chemistry. The second example focuses on a condensation reaction in monodisperse emulsions and is selected to illustrate more quantitatively how chemical equilibria observed at the macroscale change in droplets.

**4.1 Multiphase Reactions in Droplets:** Hunt *et al.*, (71) measured the reaction of O<sub>3</sub> with nitrite (NO<sub>2</sub><sup>-</sup>) in aqueous droplets (Figure 8). More generally, this example illustrates how rate constants measured under dilute beaker scale conditions are used to predict the corresponding reactivity in small droplets. The decay of nitrite when exposed to gas phase ozone is measured by Raman spectroscopy in single optically levitated droplets (71). The size of the droplet is carefully

monitored and remains nearly unchanged during the reaction. An example of the decay kinetics is shown in Figure 8A for  $[\text{NO}_2^-] = 0.2 \text{ M}$  in a  $r = 5.75 \text{ }\mu\text{m}$  aqueous droplet exposed to 12 ppm gas phase ozone.

The first step to interpret the observed kinetics is to quantify the partitioning of reactants (*i.e.*,  $\text{NO}_2^-$  and  $\text{O}_3$ ) between the droplet surface and its interior.  $K_{sb}^{\text{NO}_2^-}$  is obtained from a fit to the adsorption isotherm measured using second harmonic generation (SHG) by Otten *et al.* (72). The square root of the SHG signal vs. bulk  $[\text{NO}_2^-]$  is fit to the Langmuir (Equation 4) as shown in Figure 8B. The SHG signal is scaled to achieve the interfacial concentration measured using photoelectron spectroscopy by Brown *et al.* (73). From the fits to the data,  $K_{sb}^{\text{NO}_2^-} = 167$  ( $\Delta G_{sb} = -3.0 \text{ kcal/mol}$ ) with a maximum interface concentration ( $\frac{\Gamma_{\infty}^{\text{NO}_2^-}}{\delta}$ ) of  $2.25 \text{ M}$  ( $1.35 \times 10^{21} \text{ molec./cm}^3$ ).

The ozone concentration in the droplet is computed from the difference in solvation energy of an isolated molecule relative to its solvation at the interface and in the bulk liquid. Solvation energies are obtained from the potential of mean force required to move  $\text{O}_3$  across the air-water interface in MD simulations. An example, (51) is shown in Figure 8C. The experimental difference in solvation free energies of  $\text{O}_{3(g)}$  and  $\text{O}_{3(b)}$  is  $\Delta G_{gb} = +0.85 \text{ kcal/mol}$  (74). This corresponds to a dimensionless Henry's law or gas-bulk partitioning constant,  $K_{gb}^{\text{O}_3}$ , of 0.27. The change in solvation free energy of  $\text{O}_3$  at the interface, varies slightly across simulations methods,

(50, 51) but is generally around -1.1 kcal/mol (i.e.,  $K_{gs}^{O_3} = 8.9$ ) as illustrated in Figure 8C. The bulk to surface partitioning constant for ozone is  $K_{sb}^{O_3} = 23$  ( $\Delta G_{sb} = -1.85$  kcal/mol) (51).

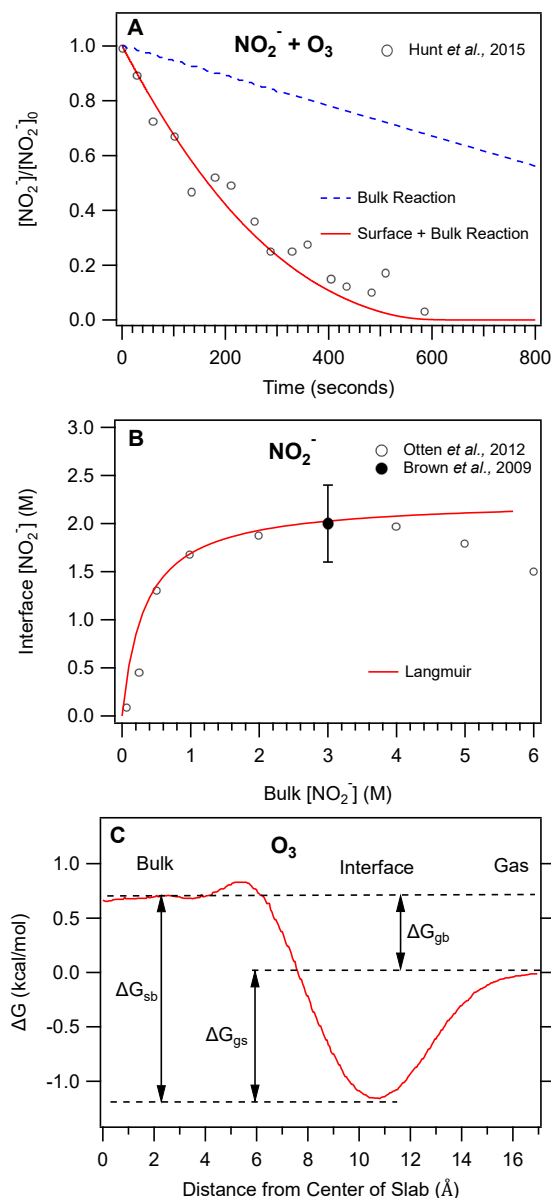


**Figure 8:** (A) Normalized decay of  $[\text{NO}_2^-]$  vs. reaction time. Experiments ( $\circ$ ) are conducted using  $[\text{O}_3] \sim 12$  ppm, a  $5.75 \mu\text{m}$  radius aqueous droplet with an initial  $[\text{NO}_2^-] = 0.2$  M as reported by Hunt *et al.* (71). Lines are kinetic simulations from Willis and Wilson (43). (B) Interfacial  $[\text{NO}_2^-]$  vs. bulk nitrite concentration. The adsorption isotherm ( $\circ$ ) is measured by Otten *et al.* (72) and the interfacial concentration ( $\bullet$ ) at bulk concentration of 3 M is measured by Brown *et al.* (73). The line is a fit of the Langmuir equation (Equation 4). (C) Solvation energy profile for  $\text{O}_3$  in water reported by Vacha *et al.* (51). The bulk region of the simulation is 0-6  $\text{\AA}$ , whereas the interface resides between 7 and 15  $\text{\AA}$ .

From  $K_{eq}^{NO_2^-}$ ,  $N_{s/b}$  is calculated to be  $2 \times 10^{-3}$  using Equations 1-5 introduced above. The adsorption length ( $L_{ads} \sim 4$  nm) is negligible compared to droplet size ( $L_{ads}/r \sim 7 \times 10^{-4}$ ). From  $N_{s/b}$  and  $L_{ads}/r$  it is expected that the interfacial and bulk concentrations will closely resemble those of a macroscale system. The critical radius (4, 43) is estimated to be  $\sim 250$  nm such that  $r > r_{crit}$  indicating that the nitrite reaction with solvated ozone in the bulk of the droplet will be limited by the liquid phase diffusion rate of  $O_3$  (43). Using a rate coefficient of  $5.6 \times 10^{-16}$  cm<sup>3</sup>/molec./s (75-79) measured in macroscale dilute aqueous solutions and a diffusion coefficient for  $NO_2^-$  ( $D = 1.42 \times 10^{-5}$  cm<sup>2</sup>/s), (80) yields  $L_{rxn} \sim 160$  nm, which is larger than the interfacial thickness but smaller than the overall size of the droplet ( $L_{rxn}/r \sim 3 \times 10^{-2}$ ). This ratio implies that unlike macroscale vessels it is likely that both surface and bulk reactions contribute to the observed heterogeneous droplet kinetics in Figure 8A.

The kinetic framework shown in Figure 1 was implemented in explicit stochastic reaction-diffusion simulations, (43) in order to predict the multiphase kinetics observed by Hunt *et al.* (71). As shown in Figure 8A, simulations that only include bulk phase reactions are too slow to replicate the droplet kinetics. This is because the bulk phase reaction rate inside the droplet, as suggested above, is limited by the liquid phase diffusion of  $O_3$  (*i.e.*,  $r > r_{crit}$ ). However, when surface reactions are included (43) the simulations replicate the experimental results. Agreement between simulation and experiment is achieved when the surface and bulk rate coefficients for the  $NO_2^- + O_3$  reaction are equal (*i.e.*,  $k_s = k_b$ )

The results presented in Figure 8 illustrate the key elementary steps needed to accurately transfer rate coefficients measured in beaker scale reactions to those same reactions occurring in microdroplets. The reaction appears to be accelerated by  $\sim 5$ x if one assumes that the reaction only occurs within the interior of the droplet, which is the most logical comparator to beaker scale

measurements. Neglecting surface reactions predicts kinetics that are too slow. It is only when the surface reactions are considered and accurate partitioning of both reagents ( $\text{O}_3$  and  $\text{NO}_2^-$ ) between the surface and bulk regions of the droplets (*c.f.*, Figures 8B and C) does the simulation accurately replicate the experimental results.

Using the partitioning constants for  $\text{O}_3$  and  $\text{NO}_2^-$  in Equation 19 predicts a microdroplet AF of  $\sim 2.7$  assuming  $k_s = k_b$ . This is close to the factor of 5 difference between bulk and surface + bulk simulations shown in Figure 8A. This difference in apparent AF (*i.e.*, 2.7 vs. 5) is due to diffusion limitations of  $\text{O}_3$ , which play a role in the observed kinetics but are not explicitly considered in Equation 19.

Partial solvation of reactants is often invoked in discussions of acceleration mechanisms (68, 81). It is interesting to note that the gas phase rate coefficient (82) ( $9 \times 10^{-11} \text{ cm}^3/\text{molec.}/\text{s}$ ) for the  $\text{O}_3 + \text{NO}_2^-$  reaction is  $10^5$  larger than in the aqueous phase (77) ( $5.6 \times 10^{-16} \text{ cm}^3/\text{molec.}/\text{s}$ ). If the surface reaction proceeded at near the gas phase reaction rate, AF's would be on the order of  $10^5$ , which is inconsistent with experimental observations and kinetic simulations. Thus, if there is a surface population of partially solvated  $\text{NO}_2^-$  near the air side of the interface reacting at or near the gas phase reaction rate it is likely too small (*i.e.*,  $N_{s/b} \ll 1$ ) to substantially influence the overall kinetic behavior of the microdroplet. Nevertheless, this is an example of a modest rate acceleration in droplets, which can only be fully understood and predicted after accurately accounting for diffusion as well as the partitioning of reagents to the microdroplet interface.

**4.2 Bimolecular Reactions in Emulsions:** Fallah-Araghi *et al.* (83) examined a condensation reaction in monodisperse micron-sized emulsions. They measured the size-dependent *in situ* formation kinetics of a fluorescent imine produced from the reaction of an amine with an aldehyde, as shown in Figure 9A. In bulk aqueous solutions, the equilibrium strongly favors reactants since

imine formation produces H<sub>2</sub>O. Yet, Fallah-Araghi *et al.* (83) observed that the imine formation rate and position of the final equilibrium was size-dependent (see Figure 9B) and enhanced relative to a macroscale solution. The equilibrium constant was observed to be 29-fold larger in  $r = 8.4$   $\mu\text{m}$  droplets compared to the bulk solution. Both the equilibrium constant and the forward rate constant ( $k_f$ ) for imine synthesis increased linearly with  $1/r$ ; signaling the importance of the interface. Fallah-Araghi *et al.* (83) developed a reaction-adsorption model to explain their results, finding that it is the weak adsorption of reagents to the oil-water interface that shifts the equilibrium and synthesis rate in small compartments.

The reacto-diffusive length for the forward synthesis rate of the imine ( $k_f$ , Figure 9A) is  $L_{rxn} \sim 3.6$  cm whereas for the backward decomposition of the imine ( $k_b$ , in Figure 9A),  $L_{rxn} \sim 580$   $\mu\text{m}$ . These lengths are much larger than the emulsion size ( $L_{rxn}/r \gg 1$ ), indicating that the interface plays a significant role in the observed microdroplet equilibrium.  $L_{ads}$  for the amine and aldehyde are 90 and 130 nm, respectively. These lengths are a fraction of the  $r = 8.4$   $\mu\text{m}$  droplet ( $L_{ads}/r \sim 10^{-2}$ ), which will only slightly alter the surface and bulk concentrations from those of a macroscale system, as discussed in Ref. (49).  $r_{crit} \sim 200$  microns, so the transport of reactants to the surface will be kinetically rather than diffusionally limited (*i.e.*,  $r < r_{crit}$ ). This kinetic limitation is nicely observed in Figure 9B where the formation kinetics of the imine are sigmoidal, unlike in a macroscale solution where the formation kinetics are exponential (49, 83). Sigmoidal kinetics appear when the timescales for reagent desolvation to the interface are competitive with reaction (49, 83).

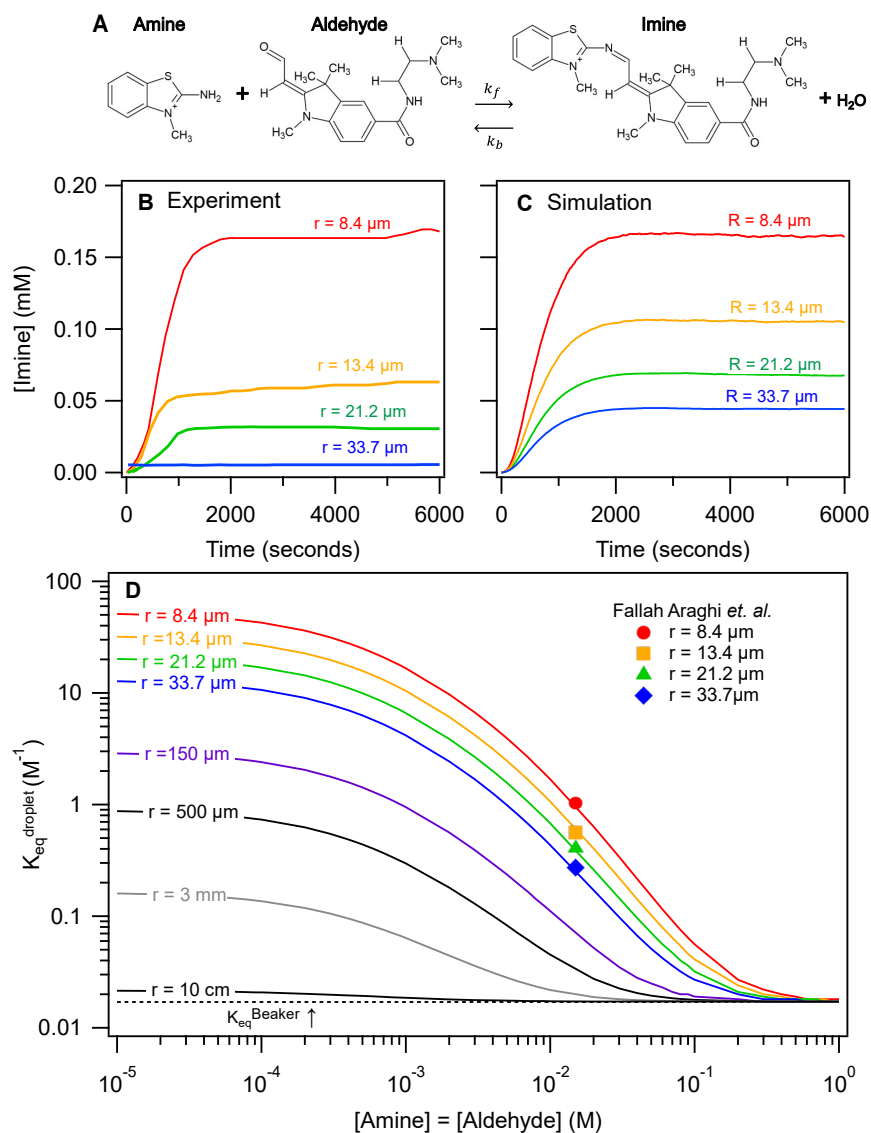


**Figure 9.** (A) Molecular structures and equilibrium for imine formation from the reaction of an amine with an aldehyde. (B) Measured imine concentration as a function of reaction time for  $r = 8.4, 13.4, 21.2$  and  $33.7 \mu\text{m}$  emulsions, as reported by Fallah-Araghi *et al.* (83). (C) Simulated imine concentration as a function of reaction time for  $r = 8.4, 13.4, 21.2$  and  $33.7 \mu\text{m}$  emulsions, as reported by Wilson *et al.* (49). (D)  $K_{eq}^{droplet}$  vs. reagent concentration and as a function of emulsion size. Data points are data from Fallah-Araghi *et al.* (83) for  $[\text{amine}] = [\text{aldehyde}] = 15 \text{ mM}$ . Lines are computed using Equation 22.  $K_{eq}^{Beaker}$  is denoted with a dashed line.

Wilson *et al.*, (49) formulated a detailed computational and theoretical model of the imine formation data measured by Fallah-Araghi *et al.*, (83) using the kinetic framework shown in Figure

1. Using a set of physically realistic rate coefficients for the partitioning and reaction of the amine and aldehyde at the emulsion interface, they were able to replicate the size dependent formation kinetics in stochastic reaction diffusion simulations as shown in Figure 9C. From the analysis of the size dependent data and simulation results, a general expression was derived to predict how the equilibrium constant at the macroscale,  $K_{eq}^{beaker}$ , is modified in microcompartments ( $K_{eq}^{droplet}$ ),

$$K_{eq}^{droplet} = K_{eq}^{Surface} \cdot N_{s/b}^{Amine} \cdot N_{s/b}^{Aldehyde} \cdot \left( \frac{r^3}{[r^3 - (r-\delta)^3]} \right) + K_{eq}^{Beaker} \quad (22)$$

$K_{eq}^{droplet}$  depends upon droplet size ( $r$ ), interface thickness ( $\delta$ ),  $K_{eq}^{Surface}$  and the fraction of reactant molecules (i.e.  $N_{s/b}^{Amine}$  and  $N_{s/b}^{Aldehyde}$ ) at the droplet interface.  $N_{s/b}^{Amine}$  and  $N_{s/b}^{Aldehyde}$  have more complex dependencies during a chemical reaction, so Equation 1 is not valid. Instead an analytical solution for  $N_{s/b}$  for a bimolecular reaction occurring via the Langmuir-Hinshelwood mechanism can be found in Ref. (49). Equation 22 has some similarities to Equation 19 developed by Ruiz-Lopez *et al.* (69) as well as to the kinetic expression developed by Valsaraj and coworkers (84) to explain accelerated gas-surface reaction rates in thin films.

Not surprisingly,  $K_{eq}^{Beaker}$  for imine synthesis is larger in organic solvents since water is a product of the reaction. Additionally, Meguellati *et al.*, (85) observed that the reaction shown in Figure 9A is enhanced inside micelles by about 60 times compared to an aqueous solution. In the model,  $K_{eq}^{Surface}$  is selected to be consistent with what is observed for micelles suggesting that the oil-water interface is a partially solvated hydrophobic environment that shifts this equilibrium towards products.

Shown in Figure 9D are predictions from Equation 22 for a range of microdroplets sizes and reactant concentrations. The experimental values of  $K_{eq}^{droplet}$  measured by Fallah-Araghi *et al.* (83) are displayed for comparison. For large droplet sizes and reagent concentrations,  $K_{eq}^{droplet} \approx K_{eq}^{beaker}$ . This is because  $N_{s/b}$  is small and approaches that of macroscale containers at large concentrations and sizes, as is illustrated in Figure 3. However, for small sizes and dilute concentrations, this first term on the RHS of Equation 22 becomes sizable and dominates the observed equilibrium constant, leading to large enhancement factors for small compartments under dilute conditions. For example,  $\frac{K_{eq}^{droplet}}{K_{eq}^{beaker}} \sim 3000$  for  $[\text{reactant}] = 10^{-5}$  M and  $r = 8.4$   $\mu\text{m}$ .

Equation 22 connects equilibria at the macro- and microscales. First, for this reaction,  $K_{eq}^{surface} > K_{eq}^{beaker}$  and reflects how the hydrophobic surface environment alters reaction energetics. While this would be true at all scales, the influence of the surface is all but obscured by the large background of bulk molecules in a beaker. The importance of this larger interfacial equilibrium constant to the overall kinetic behavior of the microdroplet is weighted by compartment size  $\left(\frac{r^3}{[r^3 - (r-\delta)^3]}\right)$  and  $N_{s/b}$ . Hence when droplets are small, and concentrations are dilute the influence of  $K_{eq}^{surface}$  is clearly manifested in the overall kinetic behavior of the droplet.

## 5. Outlook

The kinetic framework and the examples discussed above assume a kinetic continuity between macroscale reactors and microdroplets. A key question going forward is whether microdroplets are essentially “small beakers” that require additional steps to properly couple surface and bulk kinetics, or alternatively, as some have suggested, that microdroplets are somehow fundamentally different chemical entities than their larger scale analogs. For example,

there are a number of studies that indicate that microdroplets exhibit unusual acid and base catalysis and can sustain stable long range ion and pH gradients (35, 53, 54, 86-88) with superacid and basic interfaces (89). In other studies, (90) droplets are observed to have a homogeneous pH with evidence that pH is a function of droplet size and is either lower (91-93) or higher (87) than the corresponding bulk solution. It has been proposed that electric fields (94) in droplets can spontaneously produce exotic reactants or catalysts such as hydrated electrons, OH radicals, (95-99) and H<sub>2</sub>O radical cations and anions (100-103). Although, we note the controversy about the exact formation mechanism of OH (*i.e.*, H<sub>2</sub>O<sub>2</sub>) (104-107).

Another key question that is currently unresolved is whether the partially solvated environment (7) of the droplet interface is sufficiently different over a large enough length scale to substantially alter the average reaction kinetics from those occurring in a homogenous aqueous solution (*i.e.*,  $k_s$  vs  $k_b$ , Figure 1). Such a change combined with surface enrichment of reagents at the interface can certainly accelerate reaction kinetics, but questions remain as to how large and general these combined effects might be. For a substantial change in  $k_s$  to influence the overall kinetics in a microdroplet requires not only that the reactants be present in significant concentrations at the interface but also that the rate of the surface reaction must kinetically dominate over the bulk. For the NO<sub>2</sub><sup>-</sup> + O<sub>3</sub> example discussed above, ozone is present in all phases (gas, interface and bulk) and kinetic analysis of the system indicates that the bulk reaction still contributes to the observed kinetics by ~30%. The gas phase reaction rate is 10<sup>5</sup> faster than in solution suggesting that there might be a very steep gradient in the reaction rate coefficients across the interface. While this level of molecular detail (depth resolved rate coefficients) is not captured in the kinetic model presented above, it was determined that the microdroplet kinetics can be satisfactorily replicated by using an average rate coefficient at the interface that is equivalent to

the bulk, (*i.e.*,  $k_s = k_b$ ) This suggests that if there is indeed a contribution from the population of fast reacting partially solvated molecules it is simply too small to exert any substantial influence on overall kinetic behavior of the microdroplet. Further work is clearly needed to examine the consequence of partial solvation in realistic atomistic (108, 109) and kinetic models to ascertain the presence and importance of interfacial gradients in rate constants (110) and how these heterogeneities might alter microdroplet reaction kinetics.

Finally, the vast majority of reports of accelerated microdroplet reactions come from ESI-MS experiments. All three phases (gas, surface, and bulk) are kinetically active in these experiments, since there is evaporation of neutrals (solvent and reagents) and ions during the transit time of the droplets into the mass spectrometer. Since gas phase reactions, in certain cases, can be orders of magnitude faster than in solution (with the interface being somewhere in between) it is likely very difficult, as has been demonstrated in some cases, (27, 28, 30) for ESI based experiments to distinguish where the reaction occurs. Evaporative concentration of reactants alone has been shown to produce large acceleration factors,  $10^2$  - $10^7$  (28, 29).

Additionally, ESI-MS studies are very difficult to model given the complexity of the ESI process itself, (28, 111) making it challenging to test the kinetic viability of some of the acceleration mechanisms proposed in the literature. This suggests that new experiments are needed. These should be ideally amenable to kinetic modeling for which the droplet size, charge and lifetime are known quantities and chemical reactions are probed *in-situ* using spectroscopic techniques (35, 112-115). Finally, theory and computational studies are now emerging (16, 66, 116-124) to provide deeper mechanistic insight, but significantly more work will be needed going forward to ascertain how electric fields, pH gradients and partial solvation might accelerate reaction kinetics in microdroplets.

**Disclosure Statement:** The authors are not aware of any affiliations, memberships, funding, or financial holdings that might be perceived as affecting the objectivity of this review.

**Acknowledgements:** KRW is indebted to Prof. Phillip Geissler (1974-2022), UC Berkeley, for preliminary discussions about this work and his willingness to share his deep insights into the nature of solvation and reactivity at liquid interfaces. The authors would like to thank Prof. Bryan Bzdek and Dr. Allison Bain of the University of Bristol for discussions about the surface tension of small droplets. This work has been supported by the Condensed Phase and Interfacial Molecular Science Program, in the Chemical Sciences Geosciences and Biosciences Division of the Office of Basic Energy Sciences of the U.S. Department of Energy (Contract No. DE-AC02-05CH11231).

## References

1. Kolb CE, Cox RA, Abbatt JPD, Ammann M, Davis EJ, et al. 2010. An overview of current issues in the uptake of atmospheric trace gases by aerosols and clouds. *Atmos. Chem. and Phys.* 10:10561-605
2. Worsnop DR, Morris JW, Shi Q, Davidovits P, Kolb CE. 2002. A chemical kinetic model for reactive transformations of aerosol particles. *Geophys. Res. Lett.* 29:57-1--4
3. Kolb CE, Worsnop DR. 2012. Chemistry and Composition of Atmospheric Aerosol Particles. *Ann. Rev. Phys. Chem.* 63:471-91
4. Wilson KR, Prophet AM, Willis MD. 2022. A Kinetic Model for Predicting Trace Gas Uptake and Reaction. *J. Phys. Chem. A* 126:7291-308
5. Shiraiwa M, Pfrang C, Pöschl U. 2010. Kinetic multi-layer model of aerosol surface and bulk chemistry (KM-SUB): the influence of interfacial transport and bulk diffusion on the oxidation of oleic acid by ozone. *Atmos. Chem. Phys.* 10:3673-91
6. Zhong J, Kumar M, Anglada JM, Martins-Costa MTC, Ruiz-Lopez MF, et al. 2019. Atmospheric Spectroscopy and Photochemistry at Environmental Water Interfaces. *Ann. Rev. Phys. Chem.* 70:45-69
7. Wei Z, Li Y, Cooks RG, Yan X. 2020. Accelerated Reaction Kinetics in Microdroplets: Overview and Recent Developments. *Ann. Rev. Phys. Chem.* 71:31-51

8. Yan X. 2021. Emerging microdroplet chemistry for synthesis and analysis. *Int.J. Mass. Spectrom.* 468:116639
9. Kafeenah H, Jen HH, Chen SH. 2022. Microdroplet mass spectrometry: Accelerating reaction and application. *Electrophoresis* 43:74-81
10. Banerjee S, Gnanamani E, Yan X, Zare RN. 2017. Can all bulk-phase reactions be accelerated in microdroplets? *Analyst* 142:1399-402
11. Yan X, Bain RM, Cooks RG. 2016. Organic Reactions in Microdroplets: Reaction Acceleration Revealed by Mass Spectrometry. *Angew. Chem., Int. Ed.* 55:12960-72
12. Lee JK, Banerjee S, Nam HG, Zare RN. 2015. Acceleration of reaction in charged microdroplets. *Q. Rev. Biophys.* 48:437-44
13. Grommet AB, Feller M, Klajn R. 2020. Chemical reactivity under nanoconfinement. *Nat. Nanotechnol.* 15:256-71
14. Park HG, Jung Y. 2014. Carbon nanofluidics of rapid water transport for energy applications. *Chem. Soc. Rev.* 43:565-76
15. Mastalerz M. 2018. Porous Shape-Persistent Organic Cage Compounds of Different Size, Geometry, and Function. *Acc. Chem. Res.* 51:2411-22
16. Pestana LR, Hao H, Head-Gordon T. 2020. Diels–Alder Reactions in Water Are Determined by Microsolvation. *Nano Lett.* 20:606-11
17. Muñoz-Santiburcio D, Marx D. 2017. Chemistry in nanoconfined water. *Chem. Sci.* 8:3444-52
18. Goch W, Bal W. 2020. Stochastic or Not? Method To Predict and Quantify the Stochastic Effects on the Association Reaction Equilibria in Nanoscopic Systems. *J. Phys. Chem. A* 124:1421-8
19. Shon MJ, Cohen AE. 2012. Mass Action at the Single-Molecule Level. *J. Am. Chem. Soc.* 134:14618-23

20. Maioli M, Varadi G, Kurdi R, Caglioti L, Pályi G. 2016. Limits of the Classical Concept of Concentration. *J. Phys. Chem. B* 120:7438-45
21. Szymanski R, Sosnowski S, Maślanka Ł. 2016. Statistical effects related to low numbers of reacting molecules analyzed for a reversible association reaction  $A + B = C$  in ideally dispersed systems: An apparent violation of the law of mass action. *J. Chem. Phys.* 144:124112
22. Khodorkovsky Y, Rubinovich L, Polak M. 2019. Stochastic Kinetics and Equilibrium of Nanoconfined Reactions. *J. Phys. Chem. C* 123:24949-56
23. Vaida V. 2017. Prebiotic phosphorylation enabled by microdroplets. *Proc. Natl. Acad. Sci. USA* 114:12359-61
24. Nam I, Lee JK, Nam HG, Zare RN. 2017. Abiotic production of sugar phosphates and uridine ribonucleoside in aqueous microdroplets. *Proc. Natl. Acad. Sci. USA* 114:12396-400
25. Nam I, Nam HG, Zare RN. 2018. Abiotic synthesis of purine and pyrimidine ribonucleosides in aqueous microdroplets. *Proc. Natl. Acad. Sci. USA* 115:36-40
26. Holden DT, Morato NM, Cooks RG. 2022. Aqueous microdroplets enable abiotic synthesis and chain extension of unique peptide isomers from free amino acids. *Proc. Natl. Acad. Sci. USA* 119:e2212642119
27. Jacobs MI, Davis RD, Rapf RJ, Wilson KR. 2019. Studying Chemistry in Micro-compartments by Separating Droplet Generation from Ionization. *J. Am. Soc. Mass Spectrom.* 30
28. Rovelli G, Jacobs MI, Willis MD, Rapf RJ, Prophet AM, Wilson KR. 2020. A Critical Analysis of Electrospray Techniques for the Determination of Accelerated Rates and Mechanisms of Chemical Reactions in Droplets. *Chem. Sci.* 11:13026-43
29. Chen CJ, Williams ER. 2023. The role of analyte concentration in accelerated reaction rates in evaporating droplets. *Chem. Sci.* 14:4704-13

30. Gallo A, Farinha ASF, Dinis M, Emwas A-H, Santana A, et al. 2019. The chemical reactions in electrosprays of water do not always correspond to those at the pristine air–water interface. *Chem. Sci.* 10:2566-77
31. Wilkinson DJ. 2009. Stochastic modelling for quantitative description of heterogeneous biological systems. *Nat. Rev. Genet.* 10:122-33
32. McAdams HH, Arkin A. 1999. It's a noisy business! Genetic regulation at the nanomolar scale. *Trends Genet.* 15:65-9
33. Symes R, Sayer RM, Reid JP. 2004. Cavity enhanced droplet spectroscopy: Principles, perspectives and prospects. *Phys. Chem. Chem. Phys.* 6:474-87
34. Corral Arroyo P, David G, Alpert PA, Parmentier EA, Ammann M, Signorell R. 2022. Amplification of light within aerosol particles accelerates in-particle photochemistry. *Science* 376:293-6
35. Li K, Gong K, Liu J, Ohnoutek L, Ao J, et al. 2022. Significantly accelerated photochemical and photocatalytic reactions in microdroplets. *Cell Reports Physical Science* 3:100917
36. Signorell R, Goldmann M, Yoder BL, Bodi A, Chasovskikh E, et al. 2016. Nanofocusing, shadowing, and electron mean free path in the photoemission from aerosol droplets. *Chem. Phys. Lett.* 658:1-6
37. Cremer JW, Thaler KM, Haisch C, Signorell R. 2016. Photoacoustics of single laser-trapped nanodroplets for the direct observation of nanofocusing in aerosol photokinetics. *Nat. Comm.* 7:10941
38. Chen S, Wan Q, Badu-Tawiah AK. 2016. Picomole-Scale Real-Time Photoreaction Screening: Discovery of the Visible-Light-Promoted Dehydrogenation of Tetrahydroquinolines under Ambient Conditions. *Angew. Chem., Int. Ed.* 55:9345-9

39. Wilson KR, Zou S, Shu J, Rühl E, Leone SR, et al. 2007. Size-Dependent Angular Distributions of Low-Energy Photoelectrons Emitted from NaCl Nanoparticles. *Nano Lett.* 7:2014-9
40. Berg MJ, Wilson KR, Sorensen CM, Chakrabarti A, Ahmed M. 2012. Discrete dipole approximation for low-energy photoelectron emission from NaCl nanoparticles. *J. Quant. Spectrosc. Radiat. Transf.* 113:259-65
41. Ban L, Yoder BL, Signorell R. 2020. Photoemission from Free Particles and Droplets. *Ann. Rev. Phys. Chem.* 71:315-34
42. Hinsberg WD, Houle FA. 2020. Kineticope ©. <https://hinsberg.net/kineticope/>
43. Willis MD, Wilson KR. 2022. Coupled Interfacial and Bulk Kinetics Govern the Timescales of Multiphase Ozonolysis Reactions. *J. Phys. Chem. A* 126:4991-5010
44. Houle FA, Miles REH, Pollak CJ, Reid JP. 2021. A purely kinetic description of the evaporation of water droplets. *J. Chem. Phys.* 154:054501
45. Heine N, Houle FA, Wilson KR. 2017. Connecting the Elementary Reaction Pathways of Criegee Intermediates to the Chemical Erosion of Squalene Interfaces during Ozonolysis. *Environ. Sci. Technol.* 51:13740-8
46. Houle FA, Hinsberg WD, Wilson KR. 2015. Oxidation of a model alkane aerosol by OH radical: the emergent nature of reactive uptake. *Phys. Chem. Chem. Phys.* 17:4412-23
47. Liu MJ, Wiegel AA, Wilson KR, Houle FA. 2017. Aerosol Fragmentation Driven by Coupling of Acid-Base and Free-Radical Chemistry in the Heterogeneous Oxidation of Aqueous Citric Acid by OH Radicals. *J. Phys. Chem. A* 121:5856-70
48. Wiegel AA, Wilson KR, Hinsberg WD, Houle FA. 2015. Stochastic methods for aerosol chemistry: a compact molecular description of functionalization and fragmentation in the heterogeneous oxidation of squalane aerosol by OH radicals. *Phys. Chem. Chem. Phys.* 17:4398-411

49. Wilson KR, Prophet AM, Rovelli G, Willis MD, Rapf RJ, Jacobs MI. 2020. A Kinetic Description of How Interfaces Accelerate Reactions in Micro-Compartments. *Chem. Sci.* 11:8533-45
50. Viececi J, Roeselová M, Potter N, Dang LX, Garrett BC, Tobias DJ. 2005. Molecular Dynamics Simulations of Atmospheric Oxidants at the Air–Water Interface: Solvation and Accommodation of OH and O<sub>3</sub>. *J. Phys. Chem. B* 109:15876-92
51. Vacha R, Slavicek P, Mucha M, Finlayson-Pitts BJ, Jungwirth P. 2004. Adsorption of Atmospherically Relevant Gases at the Air/Water Interface: Free Energy Profiles of Aqueous Solvation of N<sub>2</sub>, O<sub>2</sub>, O<sub>3</sub>, OH, H<sub>2</sub>O, HO<sub>2</sub>, and H<sub>2</sub>O<sub>2</sub>. *J. Phys. Chem. A* 108:11573-9
52. Langmuir I. 1918. The Adsorption of Gases on Plane Surfaces of Glass, Mica and Platinum. *J. Am. Chem. Soc.* 40:1361-403
53. Chamberlayne CF, Zare RN. 2020. Simple model for the electric field and spatial distribution of ions in a microdroplet. *J. Chem. Phys.* 152:184702
54. Chamberlayne CF, Zare RN. 2022. Microdroplets can act as electrochemical cells. *J. Chem. Phys.* 156
55. Bleys G, Joos P. 1985. Adsorption kinetics of bolaform surfactants at the air/water interface. *J. Phys. Chem.* 89:1027-32
56. Jin F, Balasubramaniam R, Stebe KJ. 2004. Surfactant adsorption to spherical particles: the intrinsic length scale governing the shift from diffusion to kinetic-controlled mass transfer. *J. Adhes.* 80:773-96
57. Zhou Z, Yan X, Lai Y-H, Zare RN. 2018. Fluorescence Polarization Anisotropy in Microdroplets. *J. Phys. Chem. Lett.* 9:2928-32
58. Bzdek BR, Reid JP, Malila J, Prisle NL. 2020. The surface tension of surfactant-containing, finite volume droplets. *Proc. Natl. Acad. Sci. USA* 117:8335-43

59. Miles REH, Glerum MWJ, Boyer HC, Walker JS, Dutcher CS, Bzdek BR. 2019. Surface Tensions of Picoliter Droplets with Sub-Millisecond Surface Age. *J. Phys. Chem. A* 123:3021-9
60. Szyszkowski Bv. 1908. Experimentelle Studien über kapillare Eigenschaften der wässrigen Lösungen von Fettsäuren. *Z. Phys. Chem* 64U:385-414
61. Alvarez NJ, Walker LM, Anna SL. 2010. Diffusion-limited adsorption to a spherical geometry: The impact of curvature and competitive time scales. *Phys. Rev. E* 82:011604
62. Kuramoto Y. 1974. Effects of Diffusion on the Fluctuations in Open Chemical Systems. *Prog. Theor. Phys.* 52:711-3
63. Houle FA, Wiegel AA, Wilson KR. 2018. Predicting Aerosol Reactivity Across Scales: from the Laboratory to the Atmosphere. *Environ. Sci. Technol.* 52:13774-81
64. Limmer DT, Götz AW, Bertram TH, Nathanson GM. 2023. Molecular Insights into Chemical Reactions at Aqueous Aerosol Interfaces. *arXiv preprint arXiv:2306.13811*
65. Klein G, Born M. 1952. Mean first-passage times of Brownian motion and related problems. *Proc. R. Soc. A: Math. Phys. Eng. Sci.* 211:431-43
66. Mondal S, Acharya S, Biswas R, Bagchi B, Zare RN. 2018. Enhancement of reaction rate in small-sized droplets: A combined analytical and simulation study. *J. Chem. Phys.* 148
67. Hardy DA, Robinson JF, Hilditch TG, Neal E, Lemaitre P, et al. 2023. Accurate Measurements and Simulations of the Evaporation and Trajectories of Individual Solution Droplets. *J. Phys. Chem. B* 127:3416-30
68. Qiu L, Wei Z, Nie H, Cooks RG. 2021. Reaction Acceleration Promoted by Partial Solvation at the Gas/Solution Interface. *ChemPlusChem* 86:1362-5
69. Ruiz-López M, Martins-Costa M. 2022. Disentangling reaction rate acceleration in water microdroplets. *Phys. Chem. Chem. Phys.* 24

70. Bain RM, Pulliam CJ, They F, Cooks RG. 2016. Accelerated Chemical Reactions and Organic Synthesis in Leidenfrost Droplets. *Angew. Chem., Int. Ed.* 55:10478-82
71. Hunt OR, Ward AD, King MD. 2015. Heterogeneous oxidation of nitrite anion by gas-phase ozone in an aqueous droplet levitated by laser tweezers (optical trap): is there any evidence for enhanced surface reaction? *Phys. Chem. Chem. Phys.* 17:2734-41
72. Otten DE, Onorato R, Michaels R, Goodknight J, Saykally RJ. 2012. Strong surface adsorption of aqueous sodium nitrite as an ion pair. *Chem. Phys. Lett.* 519-520:45-8
73. Brown MA, Winter B, Faubel M, Hemminger JC. 2009. Spatial Distribution of Nitrate and Nitrite Anions at the Liquid/Vapor Interface of Aqueous Solutions. *J. Am. Chem. Soc.* 131:8354-5
74. Sander R. 2015. Compilation of Henry's law constants (version 4.0) for water as solvent. *Atmos. Chem. Phys.* 15:4399-981
75. Damschen DE, Martin LR. 1983. Aqueous aerosol oxidation of nitrous acid by O<sub>2</sub>, O<sub>3</sub> and H<sub>2</sub>O<sub>2</sub>. *Atmos. Environ.* 17:2005-11
76. Hoigné J, Bader H. 1983. Rate constants of reactions of ozone with organic and inorganic compounds in water—II: Dissociating organic compounds. *Water Res.* 17:185-94
77. Garland JA, Elzerman AW, Penkett SA. 1980. The mechanism for dry deposition of ozone to seawater surfaces. *J. Geophys. Res. Oceans* 85:7488-92
78. Liu Q, Schurter LM, Muller CE, Aloisio S, Francisco JS, Margerum DW. 2001. Kinetics and Mechanisms of Aqueous Ozone Reactions with Bromide, Sulfite, Hydrogen Sulfite, Iodide, and Nitrite Ions. *Inorg. Chem.* 40:4436-42
79. Penkett SA. 1972. Oxidation of SO<sub>2</sub> and Other Atmospheric Gases by Ozone in Aqueous Solution. *Nat. Phys. Sci.* 240:105-6
80. Yeh HS, Wills GB. 1970. Diffusion coefficient of sodium nitrate in aqueous solution at 25.deg. as a function of concentration from 0.1 to 1.0M. *J. Chem. Eng. Data.* 15:187-9

81. Kang J, Lhee S, Lee JK, Zare RN, Nam HG. 2020. Restricted intramolecular rotation of fluorescent molecular rotors at the periphery of aqueous microdroplets in oil. *Sci. Rep.* 10:16859
82. Lifshitz C, Wu RLC, Tiernan TO, Terwilliger DT. 2008. Negative ion–molecule reactions of ozone and their implications on the thermochemistry of O<sub>3</sub><sup>-</sup>. *J. Chem. Phys.* 68:247-60
83. Fallah-Araghi A, Meguellati K, Baret JC, El Harrak A, Mangeat T, et al. 2014. Enhanced Chemical Synthesis at Soft Interfaces: A Universal Reaction-Adsorption Mechanism in Microcompartments. *Phys. Rev. Lett.* 112:028301-
84. Karre AV, Valsaraj KT, Vasagar V. 2023. Review of air-water interface adsorption and reactions between trace gaseous organic and oxidant compounds. *Sci. Total Environ.* 873:162367
85. Meguellati K, Fallah-Araghi A, Baret J-C, El Harrak A, Mangeat T, et al. 2013. Enhanced imine synthesis in water: from surfactant-mediated catalysis to host–guest mechanisms. *Chem. Comm.* 49:11332-4
86. Gong K, Ao J, Li K, Liu L, Liu Y, et al. 2023. Imaging of pH distribution inside individual microdroplet by stimulated Raman microscopy. *Proc. Natl. Acad. Sci. USA* 120:e2219588120
87. Wei H, Vejerano EP, Leng W, Huang Q, Willner MR, et al. 2018. Aerosol microdroplets exhibit a stable pH gradient. *Proc. Natl. Acad. Sci. USA* 115:7272-7
88. Malevanets A, Consta S. 2013. Variation of droplet acidity during evaporation. *J. Chem. Phys.* 138
89. Huang K-H, Wei Z, Cooks RG. 2021. Accelerated reactions of amines with carbon dioxide driven by superacid at the microdroplet interface. *Chem. Sci.* 12:2242-50
90. Li M, Kan Y, Su H, Pöschl U, Parekh SH, et al. 2023. Spatial homogeneity of pH in aerosol microdroplets. *Chem* 9:1036-46

91. Craig RL, Peterson PK, Nandy L, Lei Z, Hossain MA, et al. 2018. Direct Determination of Aerosol pH: Size-Resolved Measurements of Submicrometer and Supermicrometer Aqueous Particles. *Anal. Chem.* 90:11232-9
92. Rindelaub JD, Craig RL, Nandy L, Bondy AL, Dutcher CS, et al. 2016. Direct Measurement of pH in Individual Particles via Raman Microspectroscopy and Variation in Acidity with Relative Humidity. *J. Phys. Chem. A* 120:911-7
93. Coddens EM, Angle KJ, Grassian VH. 2019. Titration of Aerosol pH through Droplet Coalescence. *J. Phys. Chem. Lett.* 10:4476-83
94. Xiong H, Lee JK, Zare RN, Min W. 2020. Strong Electric Field Observed at the Interface of Aqueous Microdroplets. *J. Phys. Chem. Lett.* 11:7423-8
95. Lee JK, Walker KL, Han HS, Kang J, Prinz FB, et al. 2019. Spontaneous generation of hydrogen peroxide from aqueous microdroplets. *Proc. Natl. Acad. Sci. USA* 116:19294-8
96. Lee JK, Han HS, Chaikasetsin S, Marron DP, Waymouth RM, et al. 2020. Condensing water vapor to droplets generates hydrogen peroxide. *Proc. Natl. Acad. Sci. USA* 117:30934-41
97. Mehrgardi MA, Mofidfar M, Zare RN. 2022. Sprayed Water Microdroplets Are Able to Generate Hydrogen Peroxide Spontaneously. *J. Am. Chem. Soc.* 144:7606-9
98. Li K, Guo Y, Nizkorodov Sergey A, Rudich Y, Angelaki M, et al. 2023. Spontaneous dark formation of OH radicals at the interface of aqueous atmospheric droplets. *Proc. Natl. Acad. Sci. USA* 120:e2220228120
99. Chen B, Xia Y, He R, Sang H, Zhang W, et al. 2022. Water–solid contact electrification causes hydrogen peroxide production from hydroxyl radical recombination in sprayed microdroplets. *Proc. Natl. Acad. Sci. USA* 119:e2209056119
100. Wang M, Gao X-F, Su R, He P, Cheng Y-Y, et al. 2022. Abundant Production of Reactive Water Radical Cations under Ambient Conditions. *CCS Chemistry* 4:1224-31

101. Qiu L, Cooks RG. 2022. Simultaneous and Spontaneous Oxidation and Reduction in Microdroplets by the Water Radical Cation/Anion Pair. *Angew. Chem., Int. Ed.* 61:e202210765
102. Ben-Amotz D. 2022. Electric buzz in a glass of pure water. *Science* 376:800-1
103. Qiu L, Morato NM, Huang K-H, Cooks RG. 2022. Spontaneous Water Radical Cation Oxidation at Double Bonds in Microdroplets. *Front. Chem.* 10:903774.
104. Gallo Jr A, Musskopf NH, Liu X, Yang Z, Petry J, et al. 2022. On the formation of hydrogen peroxide in water microdroplets. *Chem. Sci.* 13:2574-83
105. Nguyen D, Lyu P, Nguyen SC. 2023. Experimental and Thermodynamic Viewpoints on Claims of a Spontaneous H<sub>2</sub>O<sub>2</sub> Formation at the Air–Water Interface. *J. Phys. Chem. B* 127:2323-30
106. Nguyen D, Nguyen SC. 2022. Revisiting the Effect of the Air–Water Interface of Ultrasonically Atomized Water Microdroplets on H<sub>2</sub>O<sub>2</sub> Formation. *J. Phys. Chem. B* 126:3180-5
107. Musskopf NH, Gallo A, Jr., Zhang P, Petry J, Mishra H. 2021. The Air–Water Interface of Water Microdroplets Formed by Ultrasonication or Condensation Does Not Produce H<sub>2</sub>O<sub>2</sub>. *J. Phys. Chem. Lett.* 12:11422-9
108. Cruzeiro VWD, Galib M, Limmer DT, Götz AW. 2022. Uptake of N<sub>2</sub>O<sub>5</sub> by aqueous aerosol unveiled using chemically accurate many-body potentials. *Nat. Comm.* 13:1266
109. Galib M, Limmer DT. 2021. Reactive uptake of N<sub>2</sub>O<sub>5</sub> by atmospheric aerosol is dominated by interfacial processes. *Science* 371:921-5
110. Singh AN, Limmer DT. 2022. Peptide Isomerization is Suppressed at the Air–Water Interface. *J. Phys. Chem. Lett.* 13:574-9

111. Zühlke M, Koenig J, Prüfert C, Sass S, Beitz T, et al. 2023. Complex reaction kinetics of a Mannich reaction in droplets under electrospray conditions. *Phys. Chem. Chem. Phys.* 25:11732-44
112. Kim P, Continetti RE. 2021. Accelerated Keto–Enol Tautomerization Kinetics of Malonic Acid in Aqueous Droplets. *ACS Earth Space Chem.* 5:2212-22
113. Brown EK, Rovelli G, Wilson KR. 2023. pH jump kinetics in colliding microdroplets: accelerated synthesis of azamonardine from dopamine and resorcinol. *Chem. Sci.* 14:6430-42
114. Angle KJ, Neal EE, Grassian VH. 2021. Enhanced Rates of Transition-Metal-Ion-Catalyzed Oxidation of S(IV) in Aqueous Aerosols: Insights into Sulfate Aerosol Formation in the Atmosphere. *Environ. Sci. Technol.* 55:10291-9
115. Parmentier EA, Corral Arroyo P, Gruseck R, Ban L, David G, Signorell R. 2022. Charge Effects on the Photodegradation of Single Optically Trapped Oleic Acid Aerosol Droplets. *J. Phys. Chem. A* 126:4456-64
116. Heindel JP, Hao H, LaCour RA, Head-Gordon T. 2022. Spontaneous Formation of Hydrogen Peroxide in Water Microdroplets. *J. Phys. Chem. Lett.* 13:10035-41
117. Hao H, Ruiz Pestana L, Qian J, Liu M, Xu Q, Head-Gordon T. 2023. Chemical transformations and transport phenomena at interfaces. *Wiley Interdiscip. Rev. Comput. Mol. Sci.* 13:e1639
118. Hao H, Leven I, Head-Gordon T. 2022. Can electric fields drive chemistry for an aqueous microdroplet? *Nat. Comm.* 13:280
119. Martins-Costa MTC, Ruiz-López MF. 2023. Electrostatics and Chemical Reactivity at the Air–Water Interface. *J. Am. Chem. Soc.* 145:1400-6
120. Narendra N, Chen X, Wang J, Charles J, Cooks RG, Kubis T. 2020. Quantum Mechanical Modeling of Reaction Rate Acceleration in Microdroplets. *J. Phys. Chem. A* 124:4984-9

121. Consta S. 2022. Atomistic Modeling of Jet Formation in Charged Droplets. *J. Phys. Chem. B* 126:8350-7
122. Kwan V, Consta S. 2020. Bridging electrostatic properties between nanoscopic and microscopic highly charged droplets. *Chem. Phys. Lett.* 746:137238
123. Kwan V, Consta S. 2021. Molecular Characterization of the Surface Excess Charge Layer in Droplets. *J. Am. Soc. Mass Spectrom.* 32:33-45
124. Kwan V, Malevanets A, Consta S. 2019. Where Do the Ions Reside in a Highly Charged Droplet? *J. Phys. Chem. A* 123:9298-310